Calibration of the air shower energy scale of the water and air Cherenkov techniques in the LHAASO experiment

F. Aharonian,[27,28] Q. An,[4,5] Axikegu,[20] L. X. Bai,[21] Y. X. Bai,[1,3] Y. W. Bao,[15] D. Bastieri,[10] X. J. Bi,[1,2,3] Y. J. Bi,[1,3] H. Cai,[23] J. T. Cai,[10] Zhen Cao,[1,2,3,*] Zhe Cao,[4,5] J. Chang,[16] J. F. Chang,[1,3,4] B. M. Chen,[13] E. S. Chen,[1,2,3] J. Chen,[21] Liang Chen,[1,2,3] Liang Chen,[18] Long Chen,[20] M. J. Chen,[1,3] M. L. Chen,[1,3,4] Q. H. Chen,[20] S. H. Chen,[1,2,3] S. Z. Chen,[1,3] T. L. Chen,[22] X. L. Chen,[1,2,3] Y. Chen,[15] N. Cheng,[1,3] Y. D. Cheng,[1,3] S. W. Cui,[13] X. H. Cui,[7] Y. D. Cui,[11] B. Z. Dai,[24] H. L. Dai,[1,3,4] Z. G. Dai,[15] Danzengluobu,[22] D. della Volpe,[32] B. D'Ettorre Piazzoli,[29] X. J. Dong,[1,3] K. K. Duan,[16] J. H. Fan,[10] Y. Z. Fan,[16] Z. X. Fan,[1,3] J. Fang,[24] K. Fang,[1,3] C. F. Feng,[17] L. Feng,[16] S. H. Feng,[1,3] Y. L. Feng,[16] B. Gao,[1,3] C. D. Gao,[17] L. Q. Gao,[1,2,3] Q. Gao,[22] W. Gao,[17] M. M. Ge,[24] L. S. Geng,[1,3] G. H. Gong,[6] Q. B. Gou,[1,3] M. H. Gu,[1,3,4] F. L. Guo,[18] J. G. Guo,[1,2,3] X. L. Guo,[20] Y. Q. Guo,[1,3] Y. Y. Guo,[1,2,3,16] Y. A. Han,[14] H. H. He,[1,2,3] H. N. He,[16] J. C. He,[1,2,3] S. L. He,[10] X. B. He,[11] Y. He,[20] M. Heller,[32] Y. K. Hor,[11] C. Hou,[1,3] H. B. Hu,[1,2,3] S. Hu,[21] S. C. Hu,[1,2,3] X. J. Hu,[6] D. H. Huang,[20] Q. L. Huang,[1,3] W. H. Huang,[17] X. T. Huang,[17] X. Y. Huang,[16] Z. C. Huang,[20] F. Ji,[1,3] X. L. Ji,[1,3,4] H. Y. Jia,[20] K. Jiang,[4,5] Z. J. Jiang,[24] C. Jin,[1,2,3] T. Ke,[1,3] D. Kuleshov,[30] K. Levochkin,[30] B. B. Li,[13] Cong Li,[1,3] Cheng Li,[4,5] F. Li,[1,3,4] H. B. Li,[1,3] H. C. Li,[1,3] H. Y. Li,[5,16] J. Li,[1,3,4] K. Li,[1,3] W. L. Li,[17] Xin Li,[4,5] Xin Li,[20] X. R. Li,[1,3] Y. Li,[21] Y. Z. Li,[1,2,3] Zhe Li,[1,3] Zhuo Li,[9] E. W. Liang,[12] Y. F. Liang,[12] S. J. Lin,[11] B. Liu,[5] C. Liu,[1,3] D. Liu,[17] H. Liu,[20] H. D. Liu,[14] J. Liu,[1,3] J. L. Liu,[19] J. S. Liu,[11] J. Y. Liu,[1,3] M. Y. Liu,[22] R. Y. Liu,[15] S. M. Liu,[20] W. Liu,[1,3] Y. Liu,[10] Y. N. Liu,[6] Z. X. Liu,[21] W. J. Long,[20] R. Lu,[24] H. K. Lv,[1,3] B. Q. Ma,[9] L. L. Ma,[1,3,‡] X. H. Ma,[1,3] J. R. Mao,[25] A. Masood,[20] Z. Min,[1,3] W. Mitthumsiri,[33] T. Montaruli,[32] Y. C. Nan,[17,‖] B. Y. Pang,[20] P. Pattarakijwanich,[33] Z. Y. Pei,[10] M. Y. Qi,[1,3] Y. Q. Qi,[13] B. Q. Qiao,[1,3] J. J. Qin,[5] D. Ruffolo,[33] V. Rulev,[30] A. Sáiz,[33] L. Shao,[13] O. Shchegolev,[30,31] X. D. Sheng,[1,3] J. Y. Shi,[1,3] H. C. Song,[9] Yu. V. Stenkin,[30,31] V. Stepanov,[30] Y. Su,[16] Q. N. Sun,[20] X. N. Sun,[12] Z. B. Sun,[8] P. H. T. Tam,[11] Z. B. Tang,[4,5] W. W. Tian,[2,7] B. D. Wang,[1,3] C. Wang,[8] H. Wang,[20] H. G. Wang,[10] J. C. Wang,[25] J. S. Wang,[19] L. P. Wang,[17] L. Y. Wang,[1,3] R. N. Wang,[20] W. Wang,[11] W. Wang,[23] X. G. Wang,[12] X. J. Wang,[1,3] X. Y. Wang,[15] Y. Wang,[20] Y. D. Wang,[1,3] Y. J. Wang,[26,§] Y. P. Wang,[1,2,3] Z. H. Wang,[21] Z. X. Wang,[24] Zhen Wang,[19] Zheng Wang,[1,3,4] D. M. Wei,[16] J. J. Wei,[16] Y. J. Wei,[1,2,3] T. Wen,[24] C. Y. Wu,[1,3] H. R. Wu,[1,3] S. Wu,[1,3] W. X. Wu,[20] X. F. Wu,[16] S. Q. Xi,[1,3] J. Xia,[5,16] J. J. Xia,[20] G. M. Xiang,[2,18] D. X. Xiao,[22] G. Xiao,[1,3] H. B. Xiao,[10] G. G. Xin,[23] Y. L. Xin,[20] Y. Xing,[18] D. L. Xu,[19] R. X. Xu,[9] L. Xue,[17] D. H. Yan,[25] J. Z. Yan,[16] C. W. Yang,[21] F. F. Yang,[1,3,4] J. Y. Yang,[11] L. L. Yang,[11] M. J. Yang,[1,3] R. Z. Yang,[5] S. B. Yang,[24] Y. H. Yao,[21] Z. G. Yao,[1,3] Y. M. Ye,[6] L. Q. Yin,[1,3] N. Yin,[17] X. H. You,[1,3] Z. Y. You,[1,2,3] Y. H. Yu,[17] Q. Yuan,[16] H. D. Zeng,[16] T. X. Zeng,[1,3,4] W. Zeng,[24] Z. K. Zeng,[1,2,3,†] M. Zha,[1,3] X. X. Zhai,[1,3] B. B. Zhang,[15] H. M. Zhang,[15] H. Y. Zhang,[17] J. L. Zhang,[7] J. W. Zhang,[21] Lu Zhang,[13] Li Zhang,[24] L. X. Zhang,[10] P. F. Zhang,[24] P. P. Zhang,[13] R. Zhang,[5,16] S. R. Zhang,[13] S. S. Zhang,[1,3] X. Zhang,[15] X. P. Zhang,[1,3] Y. F. Zhang,[20] Y. L. Zhang,[1,3] Yong Zhang,[1,3] Yi Zhang,[1,16] B. Zhao,[20] J. Zhao,[1,3] L. Zhao,[4,5] L. Z. Zhao,[13] S. P. Zhao,[16,17] F. Zheng,[8] Y. Zheng,[20] B. Zhou,[1,3] H. Zhou,[19] J. N. Zhou,[18] P. Zhou,[15] R. Zhou,[21] X. X. Zhou,[20] C. G. Zhu,[17] F. R. Zhu,[20] H. Zhu,[7] K. J. Zhu,[1.2.3.4] and X. Zuo[1,3]

(LHAASO Collaboration)

[1]*Key Laboratory of Particle Astrophysics & Experimental Physics Division & Computing Center, Institute of High Energy Physics, Chinese Academy of Sciences, 100049 Beijing, China*
[2]*University of Chinese Academy of Sciences, 100049 Beijing, China*
[3]*TIANFU Cosmic Ray Research Center, Chengdu, Sichuan, China*
[4]*State Key Laboratory of Particle Detection and Electronics, China*
[5]*University of Science and Technology of China, 230026 Hefei, Anhui, China*
[6]*Department of Engineering Physics, Tsinghua University, 100084 Beijing, China*
[7]*National Astronomical Observatories, Chinese Academy of Sciences, 100101 Beijing, China*
[8]*National Space Science Center, Chinese Academy of Sciences, 100190 Beijing, China*
[9]*School of Physics, Peking University, 100871 Beijing, China*
[10]*Center for Astrophysics, Guangzhou University, 510006 Guangzhou, Guangdong, China*
[11]*School of Physics and Astronomy & School of Physics (Guangzhou), Sun Yat-sen University, 519082 Zhuhai, Guangdong, China*
[12]*School of Physical Science and Technology, Guangxi University, 530004 Nanning, Guangxi, China*
[13]*Hebei Normal University, 050024 Shijiazhuang, Hebei, China*
[14]*School of Physics and Microelectronics, Zhengzhou University, 450001 Zhengzhou, Henan, China*
[15]*School of Astronomy and Space Science, Nanjing University, 210023 Nanjing, Jiangsu, China*

[16]*Key Laboratory of Dark Matter and Space Astronomy, Purple Mountain Observatory, Chinese Academy of Sciences, 210023 Nanjing, Jiangsu, China*
[17]*Institute of Frontier and Interdisciplinary Science, Shandong University, 266237 Qingdao, Shandong, China*
[18]*Key Laboratory for Research in Galaxies and Cosmology, Shanghai Astronomical Observatory, Chinese Academy of Sciences, 200030 Shanghai, China*
[19]*Tsung-Dao Lee Institute & School of Physics and Astronomy, Shanghai Jiao Tong University, 200240 Shanghai, China*
[20]*School of Physical Science and Technology & School of Information Science and Technology, Southwest Jiaotong University, 610031 Chengdu, Sichuan, China*
[21]*College of Physics, Sichuan University, 610065 Chengdu, Sichuan, China*
[22]*Key Laboratory of Cosmic Rays (Tibet University), Ministry of Education, 850000 Lhasa, Tibet, China*
[23]*School of Physics and Technology, Wuhan University, 430072 Wuhan, Hubei, China*
[24]*School of Physics and Astronomy, Yunnan University, 650091 Kunming, Yunnan, China*
[25]*Yunnan Observatories, Chinese Academy of Sciences, 650216 Kunming, Yunnan, China*
[26]*College of Sciences, Northeastern University, 110819 Shenyang, Liaoning, China*
[27]*Dublin Institute for Advanced Studies, 31 Fitzwilliam Place, 2 Dublin, Ireland*
[28]*Max-Planck-Institut for Nuclear Physics, P.O. Box 103980, 69029 Heidelberg, Germany*
[29]*Dipartimento di Fisica dell'Università di Napoli "Federico II", Complesso Universitario di Monte Sant'Angelo, via Cinthia, 80126 Napoli, Italy*
[30]*Institute for Nuclear Research of Russian Academy of Sciences, 117312 Moscow, Russia*
[31]*Moscow Institute of Physics and Technology, 141700 Moscow, Russia*
[32]*Département de Physique Nucléaire et Corpusculaire, Faculté de Sciences, Université de Genève, 24 Quai Ernest Ansermet, 1211 Geneva, Switzerland*
[33]*Department of Physics, Faculty of Science, Mahidol University, 10400 Bangkok, Thailand*

(Received 2 June 2021; accepted 11 August 2021; published 15 September 2021)

The Wide Field-of-View Cherenkov Telescope Array (WFCTA) and the Water Cherenkov Detector Array (WCDA) of LHAASO are designed to work in combination for measuring the energy spectra of the cosmic ray species over a very wide energy range from a few TeV to 10 PeV. The energy calibration can be achieved with a proven technique of measuring the westward shift of the Moon shadow cast by galactic cosmic rays due to the geomagnetic field. This deflection angle Δ is inversely proportional to the cosmic ray rigidity. The precise measurement of the shifts by WCDA allows us to calibrate its energy scale for energies as high as 35 TeV. Through a set of commonly triggered events, the energy scales can be propagated to WFCTA. The energies of the events can be derived both by WCDA-1 and WFCTA with the median energies $23.4 \pm 0.1 \pm 1.3$ TeV and $(21.9 \pm 0.1$ TeV), respectively, which are consistent within uncertainties. In addition, the propagation of the energy scale is also validated by the Moon shadow based on the same data selection criteria of the commonly triggered events. This paper reports, for the first time, an observational measurement of the absolute energy scale of the primary cosmic rays generating showers observed by air Cherenkov telescopes.

DOI: 10.1103/PhysRevD.104.062007

I. INTRODUCTION

Cosmic ray experiments based on the extensive air shower (EAS) technique usually feature different types of ground-based detectors, such as a scintillation counter array, water Cherenkov detectors, or imaging air Cherenkov telescopes, each measuring shower properties in different ways. A combination of those measurements using different techniques will provide a rather full observation of the shower development in the atmosphere, thus a good measurement of the shower energy and the primary composition of incident cosmic ray particle, if the muon content is also measured. The Large High Altitude Air Shower Observatory (LHAASO) is such a hybrid detector array for the purpose of charged cosmic ray measurements. It has an advantage of cross-checking the shower energy measurements between the different ways by using different detector components of the array. In cosmic ray studies, it is also important the possibility of propagating the absolute energy from lower energies, at which the calibrations are done usually, to higher energies, e.g., the "knee"

*caozh@ihep.ac.cn
†zengzk@ihep.ac.cn
‡llma@ihep.ac.cn
§wangyanjin@ihep.ac.cn
‖nanyc@ihep.ac.cn

region. In direct cosmic ray measurements with single detector in space, the calibration can be performed before launch at CERN with the 350 GeV proton beam. For ground-based array of detectors and telescopes, there is no artificial test beam for the calibration. Therefore, it is mandatory to establish a way to calibrate the shower energy measurement directly using cosmic ray data. It is a nontrivial task, however, it has been done by many experiments, such as ARGO-YBJ [1], that successfully calibrated their energy scale by using the Moon shadow of cosmic rays, that is the deficit of cosmic rays blocked by the Moon as it moves inside the field of view (FoV) of the detectors. The Moon shadow can be used as a test beam because of the energy dependent deflection of cosmic rays in the geomagnetic field (GMF) [2] that shifts the Moon shadow on the ground with respect to the Moon real position. The displacement of the shadow is clearly dependent on the cosmic ray rigidity and is also dependent on the knowledge of the cosmic ray composition. Given the strength of GMF, this method is only available below tens of TeV because the shift becomes so small at higher energies that cannot be measured. Below 100 TeV, CREAM [3] and DAMPE [4,5] have measured the fluxes of protons, Helium nuclei and other light components. The measurements of CREAM and DAMPE enable the LHAASO experiment to calibrate its absolute energy scale with a small systematic uncertainty caused by the compositions. For the Wide Field-of-view Cherenkov Telescope Array (WFCTA), the faint Cherenkov light is overwhelmed by moonlight, and cannot be detected near the direction of the Moon. The WFCTA energy scale is then impossible to be directly calibrated with this method. However, the Water Cherenkov Detector Array (WCDA) is suitable to be calibrated by using the Moon shadow shifts. The calibrated energy scale at as high as possible energies has to be propagated to WFCTA by means of crossing calibration between the arrays. In this paper, we present the results of measurement of the energy scale using one of the ponds of WCDA, denoted as WCDA-1, and the propagation of the energy scale to WFCTA, which is the core detector array responsible to the energy reconstruction in the hybrid measurements of the spectra of cosmic rays in a higher energy range in which the knees locate.

WCDA has a detection threshold of about 1 TeV for charged cosmic rays [6,7]. It has measured the Moon shadow shifts as a function of $N_{\rm hit}$ as shown in Fig. 1. Here, Δ is the displacement of the centroid of the deficits of cosmic rays in the Moon shadow from the real position of the Moon and $N_{\rm hit}$ is the number of triggered detector units with trigger time within 30 ns from the conical front of a shower. To accurately measure the location of the Moon shadow, we need a reconstruction of arrival directions of showers at certain resolution which is described in Ref. [7]. Second, we need sufficient statistics for a well-established shadow of the Moon, namely the significance of the Moon

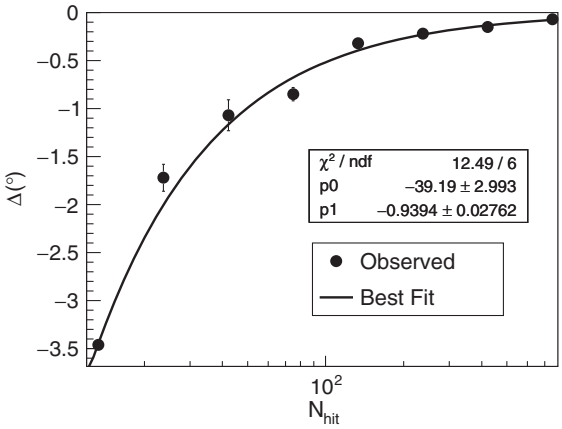

FIG. 1. The displacement of the Moon shadow from the real direction of the Moon as a function of $N_{\rm hit}$.

shadow for each $N_{\rm hit}$ group is required to be greater than 10σ. The measured deflection can be clearly seen as large as 3.5° for small showers and less than 0.3° for large showers with more than 200 hits. The displacements can be approximated by the simple form $\Delta = p0 \cdot N_{\rm hit}^{p1}$, where $p0 = -39.2 \pm 2.9$ and $p1 = -0.939 \pm 0.028$. For small showers, the energy is estimated using $N_{\rm hit}$ as described in Ref. [7] for gamma-rays below 12 TeV. At the same time, the shadow shift can be evaluated using a ray tracing algorithm with a detailed GMF model [2] and for given cosmic ray compositions, i.e., a mixture with different ratios of protons and Helium nuclei as a function of their energies. Using a detailed simulation of shower development and detector responses, one can reproduce the form of Δ vs $N_{\rm hit}$ in principle, thus establish a correlation between $N_{\rm hit}$ and shower primary energy. However, in this paper, we choose not to do so, but only focus on the high energy showers with at least $N_{\rm hit} > 200$, because the charged cosmic ray measurements will be done mainly above 100 TeV. This requires the calibration at energies as high as possible. The other reason of the choice of the high energy range is that the WCDA response to showers becomes simple because those showers are far above the trigger threshold, thus minimizing the systematic issues such as the composition and hadronic interaction models in the simulation. However, at such high energies, $N_{\rm hit}$ is no longer to be suitable as the shower energy estimator because of the natural saturation effect due to the limits of the total number of units in the pond [7]. In this paper we use the total number of recorded photoelectrons in an event, $N_{\rm pe}$ as the energy estimator for showers above 6 TeV, at which no absolute energy calibration has been done before by any experiment.

WFCTA measures the Cherenkov light generated by secondary particles produced in the atmosphere. By imaging the whole shower development, the accumulated Cherenkov light generated since the beginning of the shower are measured. The shower energy and the

atmospheric depth at which the shower reaches the maximum can be derived from the image. However, there is no direct absolute calibration method for the telescopes. In this paper, we present a propagation of the energy scale measured by WCDA to WFCTA by means of a commonly triggered cosmic ray events. Due to the area of the mirrors of each telescope is about 5 m^2, the energy threshold of WFCTA is higher than that of WCDA, only events with energies above 15 TeV can be used for this cross-calibration. At such high energies, the real challenge lies in the fact that the shift of the Moon shadow becomes small and, at the same time, the number of events for this measurement decreases with energy as well. Therefore, at this early stage of the LHAASO experiment, it is found that the limited statistics is the dominant uncertainty in this calibration procedure. Clearly, accumulating data over time, the statistical error will be reduced until it becomes less important than the systematic uncertainties due to the unknown composition of the cosmic rays and the hadronic interaction models used to simulate showers. The overall uncertainty of the energy scale should become lower than 10% after four years of observation.

We briefly describe the detectors in the LHAASO Observatory in Sec. II of this paper. In Sec. III, we discuss how the energy scale for WCDA-1 is established using the Moon shadow shift measurements for energies above 6 TeV, including the definition of a suitable energy estimator and the ray-tracing calculation. The uncertainties of the energy scale are also discussed in this section.

How the WCDA-1 energy scale is propagated to WFCTA for calibrating the reconstruction of shower energies is described in Sec. IV. We described how to select the set of commonly triggered events, how well the two energy estimations, using WCDA and WFCTA, agree with each other, recalibrating the energy scale by using a subset of data that matches the commonly triggered dataset better than the whole set for the Moon shadow measurements. Finally, we compared the energy scale with the reconstructed energies of showers by using WFCTA, and the uncertainty analysis of the energy scale. We draw conclusions in Sec. V.

II. THE LHAASO WCDA AND WFCTA ARRAYS

The LHAASO Observatory is based on the so-called "hybrid" approach for the measurement of shower characteristics, consisting in the simultaneous detection of atmospheric showers with different types of detectors. The observatory is built around the three ponds of water Cherenkov Detector Array (WCDA), featuring 3120 gap-less detecting units to instrument an area of 78,000 m^2. Near WCDA, 18 wide field of view Cherenkov telescopes (WFCTA) are installed. They survey the sky above the whole array with a coverage of 4608 square degrees [6,8]. The core of the array is surrounded by 5195 scintillation counters (ED) and 1188 muon detectors (MD),

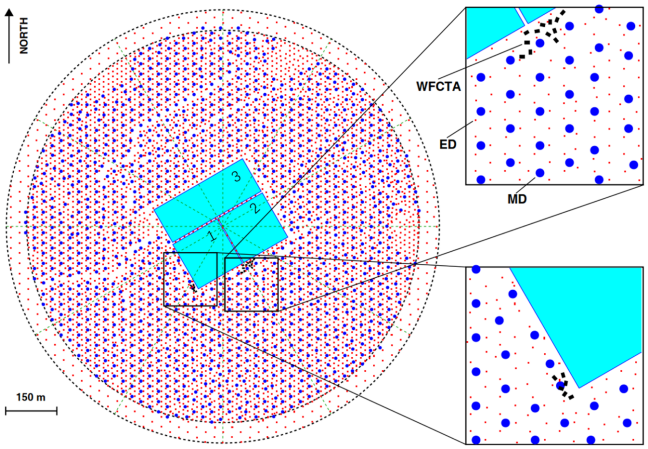

FIG. 2. The LHAASO layout. The three ponds of WCDA are represented by the cyan rectangles at the center of the site. The 6 WFCTA telescopes, positioned near the southwest core of WCDA-1, can be seen in the zoomed view at the bottom right. The remaining KM2A extends over an area of about 1 km^2, instrumented with the electromagnetic detector (ED) array of scintillation counters (small red dots) and the muon detector array (big blue dots).

which constitute an array covering an area of 1 km^2 (KM2A) [6,8,9].

As shown in Fig. 2, the WCDA is composed of two ponds with an area of 150 m × 150 m each and a third larger one with an area of 300 m × 110 m. The smaller pond in the southwest direction, named WCDA-1, has started science operations since April 2019. It has 900 units, or cells, of 25 m^2, each equipped with a large (8″) PMT used also for timing and a small (1.5″) PMT at the center of each unit at 4.4 m of depth from the water surface. The use of two PMTs watching upwards allows us to cover a wide dynamic range spanning from 1 to 200,000 photoelectrons, which are generated by the Cherenkov light produced in water by the shower charged secondary particles. To suppress the light cross-talking effect and improve the timing resolution, black plastic curtains delimit the units. The front-end electronics (FEE) of the large PMTs is designed to achieve a time resolution of 0.5 ns enough to reconstruct the shower front conical structure. The large dynamic range provided by the combined operation of PMTs (see Fig. 3) enables the measurement of the particle density distribution in the shower cores without any saturation even for energetic showers up to 10 PeV. This allows to measure the core location with a precision better than 3 m over a wide energy range up to 10 PeV. WCDA-1 can measure shower directions with a resolution better than 0.2° above 10 TeV and 1.0° above 600 GeV [7]. The water transmission can be monitored by the "muon" peak observed by each unit [7].

WFCTA is composed of 18 telescopes. In the quarter array stage of LHAASO, six telescopes are installed and located in the Southwest corner of WCDA-1 to achieve the

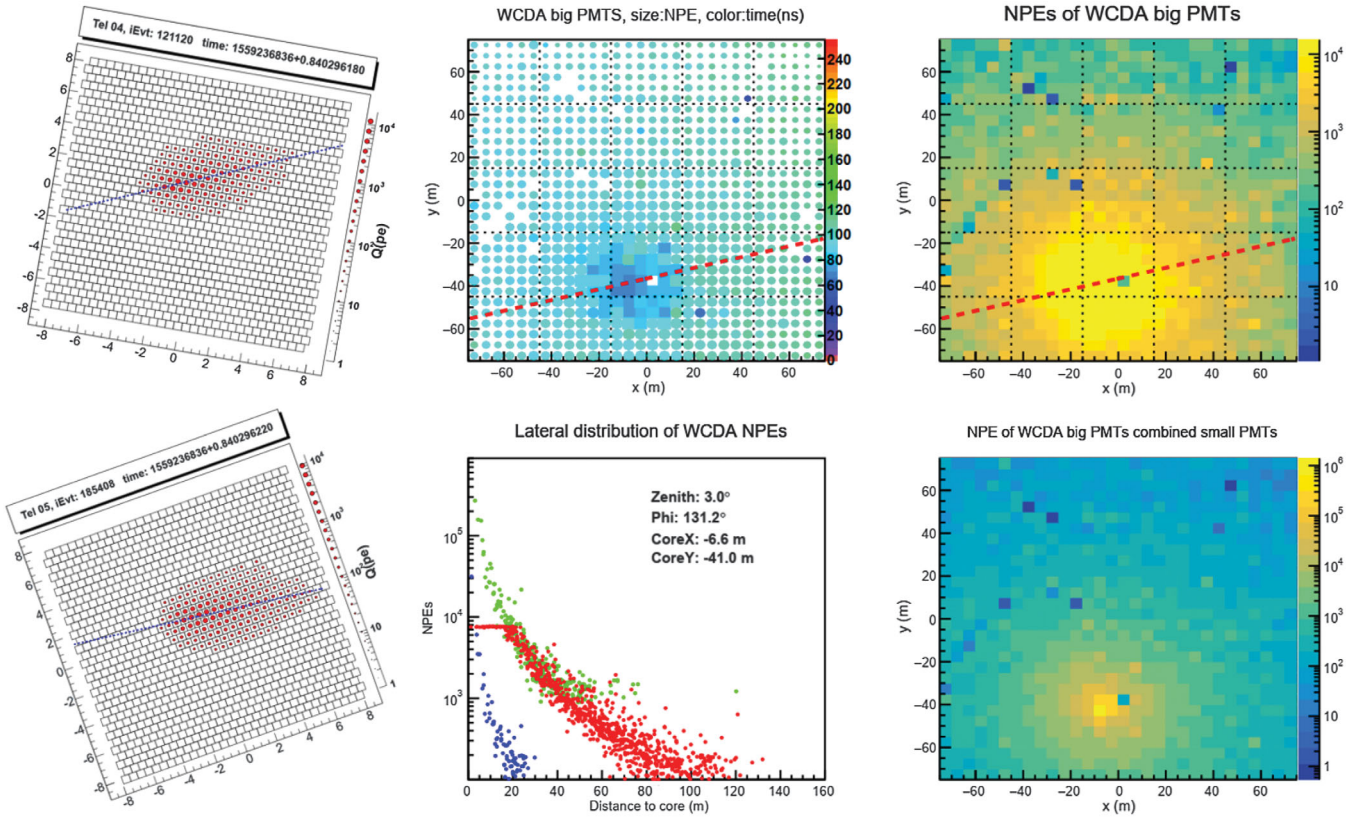

FIG. 3. A typical event that triggered both WCDA-1 and WFCTA. The two panels on the left-hand side show the images recorded by two of the WFCTA telescopes, both in vertical view, but with different orientations of 15° and 45°, respectively, from north toward west. The two panels on the right, instead, show the maps of hits in WCDA-1 units, where the color scale indicates the number of recorded photo-electrons (N_{pe}). The top right panel shows the map for the 8″ PMTs, which exhibit a clear saturation in the central region of the shower. The lower right panel shows the map for the same event as recorded by the 1.5″ PMTs. The corresponding lateral distributions of N_{pe} are shown in the lower panel in the middle column. Here, the red dots represent the 8″ PMT and the blue ones the 1.5″ PMTs, which are also scaled (green dots) and overlaid on the previous one to reconstruct the profile over the full range. The upper panel in the middle column shows the arrival time (in ns) of shower secondary particles as recorded by the WCDA-1.

hybrid observation with WCDA and KM2A by offline trigger. The centers of the six telescopes are located 100 m south and 38.5 west of the WCDA-1 center, as shown in Fig. 2 by the zoomed view bottom right. Another 12 telescopes have been built completely before October 2020, which are located the side of WCDA-1 and WCDA-2 as shown in Fig. 2 by the zoomed view up right. The telescopes have mirrors with an area of about 5 m^2, composed of aluminized spherical mirror facets. Each telescope can be tilted in elevation from 0° to 90°. A camera with 32×32 square pixels, realizing a FoV of $16° \times 16°$, is in the focal plane of the telescope, at 2870 mm away from the mirror center. Each pixel is realized by a silicon photomultiplier (SiPM) coupled to a square-surface light-funnel of 1.5 cm × 1.5 cm, corresponding to a FoV of $0.5° \times 0.5°$. Each SiPM is composed by an array of 0.36 million avalanche photo diodes (APDs) with a micro-cell size of 25 μm, covering a dynamic range from 10 to 32,000 photo-electrons [10]. In front of the photo-sensors and light-funnels, a window is installed. The window is coated with a wide-band filter to suppress the light above 550 nm, where the night sky background light (NSB) dominates with respect to the Cherenkov signal [11]. This is relevant since the photodetection sensitivity of SiPMs is considerably larger than PMT one at these wavelengths. The performance of SiPM is affected by the temperature and night sky background [12]. A calibrated LED system is installed in front of the camera to calibrate the performance of SiPMs in real time.

Each group of 16 pixels is clustered together in a FEE board connected with the readout system. Each pixel has a high-gain and a low-gain channel, each equipped with a 50 MHz 12-bit flash ADC to digitize the waveform. These two channels allow to cover the whole dynamic range of the SiPMs. A trigger signal, T_0, is generated by the high-gain channel of each pixel and transmitted to the trigger logic that collects the signals from all pixels. A pattern recognition algorithm is used to decide whether or not a shower has been observed. It generates a signal T_1, which starts the readout of the digital waveform from every pixel. The total charge and the average time of the waveform are transmitted to the LHAASO data center with an absolute time

stamp. Further offline triggers, in particular the inter-telescope trigger, and noise pixel rejection are carried out on the CPUs of the data center. A typical common trigger event with WCDA-1 and two telescopes is shown in Fig. 3.

III. DETERMINATION OF THE ENERGY SCALE OF WCDA-1

As noticed in the previous sections, the energy range where WCDA-1 and WFCTA can observe the same showers corresponds to the highest energy range for WCDA-1 where the use of $N_{\rm hit}$ as energy proxy is prevented by its saturation. Counting the number of detector units triggered during an air shower event may lead to a lack of dynamic range. In its place, the total number $N_{\rm pe}$ of photoelectrons from the PMTs measured in all units can be used as a proxy for the energy. Indeed, $N_{\rm pe}$ depends on the number of shower secondary particles hitting each unit and on their energy, thus enabling a simple form $E = bN_{\rm pe}^{\beta}$ to relate it to the energy of the primary cosmic ray inducing the shower. Since the combination of the charge output of the two PMTs covers a wide dynamic range in terms of photoelectrons, from 1 to 200,000, $N_{\rm pe}$ may represent a robust estimator up to very high energies [7].

The energy scale of WCDA-1 can be obtained according to the following steps:

(1) Selecting the total number of photo-electron detected by PMTs, $N_{\rm pe}$, and measuring the Moon shadow shift westward as a function of $N_{\rm pe}$, i.e., Δ vs $N_{\rm pe}$.
(2) Calculating the Moon shadow shifts by tracing the cosmic rays with certain composition through GMF as a function of primary cosmic ray energy, i.e., Δ vs energy.
(3) Investigating the composition of cosmic ray events that trigger WCDA-1 in the relevant ranges of $N_{\rm pe}$ using the air shower and detector response simulation. The composition is used as an input to establish the adequate relation between the measured Δ and the primary energy.
(4) Establishing the energy scale, namely $N_{\rm pe}$ versus $E_{\rm median}$ in each group of $N_{\rm pe}$.
(5) Investigating the effect due to the shower energy resolution and the power-law like CR spectrum to the match between $N_{\rm pe}$ and the primary energy according to the corresponding Moon shadow shift.

A. $N_{\rm pe}$ as the energy estimator for high energy showers

As previously stated, the simple form relating the primary energy to its estimator is $E = bN_{\rm pe}^{\beta}$ where the parameters b and β, can be determined by fitting the measured Moon shadow shifts. Here $N_{\rm pe}$ is the total number of photoelectrons measured by units with trigger time within 30 ns from the shower conical front.

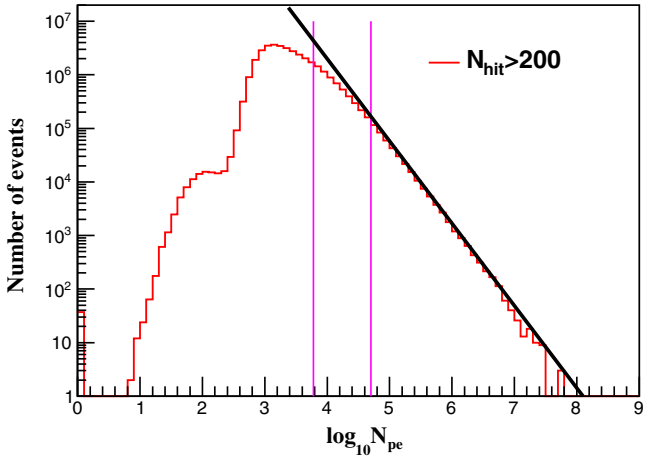

FIG. 4. The distribution of the total number of photoelectrons, $N_{\rm pe}$, for shower events coming from a region around the normal Moon position. The black solid line indicates a power law $\propto N_{\rm pe}^{-2.6}$, which fits the histograms for $N_{\rm pe} > 50{,}000$. The two vertical magenta lines indicate the range used for the energy calibration using the Moon shadow.

In Fig. 4 the distribution of $N_{\rm pe}$ is shown for the events with $N_{\rm hit}$ greater than 200 used in the Moon shadow analysis. Showers reconstructed in WCDA-1 with $N_{\rm hit}$ more than 200 have a rather good angular resolution 0.39° [7]. From Fig. 4 we can infer that above a certain energy, corresponding to $N_{\rm pe} > 50{,}000$, the showers are detected by WCDA-1 with a constant efficiency. As a matter of fact, the distribution of $N_{\rm pe}$ has a clear power law behavior between 50,000 to 10^6 with a power index of -2.6, which is the same as the spectral index of the proton spectrum measured around 13 TeV by DAMPE [4]. This indicates that the efficiency keeps constant in this energy range, and $N_{\rm pe}$ is a good indicator of the energy.

B. Measurement of Moon shadow shifts for high energy showers

The dataset in this analysis was collected from 01/05/2019 to 31/01/2020. The total effective observation time of the Moon with zenith angles smaller than 45° is 731.2 hours and the total number of events is about 4.17 million with arrival direction within 5° to the normal Moon position. To measure the deflection angle as a function of the energy, events are grouped into six groups according to $N_{\rm pe}$ as shown in Table I. During the significance analysis, only events with zenith angles $< 45°$ and $N_{\rm hit} > 200$ are used.

For the dataset in each group, the sky map in celestial coordinates near the moon region is divided into a grid of $0.02° \times 0.02°$ bins and filled with detected events according to their reconstructed arrival directions.The number of background in each grid is estimated by the equal zenith method [13]. The deficit significance in each grid is

TABLE I. Moon shadow shifts in RA, the significance of the Moon shadow, and the reconstructed median energy with its error, for each N_{pe} bin.

Range of N_{pe}	Shift of the Moon shadow (°)	Significance (σ)	Median E (TeV)
6,000–10,000	-0.32 ± 0.04	18.2	$6.6^{+0.9}_{-0.7}$
10,000–15,000	-0.25 ± 0.04	14.0	$8.4^{+1.6}_{-1.2}$
15,000–20,000	-0.15 ± 0.04	11.6	$14.0^{+5.1}_{-2.9}$
20,000–30,000	-0.11 ± 0.03	11.9	$19.1^{+7.2}_{-4.1}$
30,000–60,000	-0.06 ± 0.03	10.8	$35.0^{+35}_{-11.6}$
>60,000	-0.01 ± 0.03	10.9	>50.0

estimated by the Li & Ma formula [14]. The maximum deficit significance around the Moon region in each N_{pe} group is shown in Table I, where the corresponding Moon shadow westward shifts with respect to the normal Moon position and uncertainties are also listed.

The six Moon shadow maps with the significance of the deficit are shown in Fig. 5 as a function of the arrival direction in right ascension (RA) and declination (Dec). For the N_{pe} group with $N_{pe} > 60{,}000$ (the last plot in Fig. 5), a significance as high as 10.9σ can be achieved. The significance map can be fitted by a bidimensional Gaussian function to determine the location of the shadow center. Its shift with respect to the normal Moon position is $0.05° \pm 0.03°$ in the Dec direction. The position of the shadow in this direction is not in the center mainly because of the pointing accuracy of the detector. The shifts measured in the RA directions are quoted in Table I for all N_{pe} groups; in the last group ($N_{pe} > 60{,}000$) the shift resulted $0.01° \pm 0.03°$.

The statistical uncertainty is the dominant contribution given the limited statistics. The standard deviation σ of the Gaussian function is found to be $0.33° \pm 0.05°$, which is the result of the combination of the size of the Moon (angular extension 0.25°) and the angular resolution of the detector [7]. The deficit number of events contained in the angular region $\sigma^2_{DEC} + \sigma^2_{RA} < 2\sigma^2$ is about 63% of the total deficit number, a value that is consistent with the simulation. For lower energies, the shadow shifts toward the west and its size increases as well, indicating a worsening of the angular resolution.

C. Calculation of Moon shadow shifts by ray-tracing in GMF

The expected Moon shadow shift westward has been calculated by using a ray-tracing simulation which propagates protons and Helium nuclei coming from the Moon

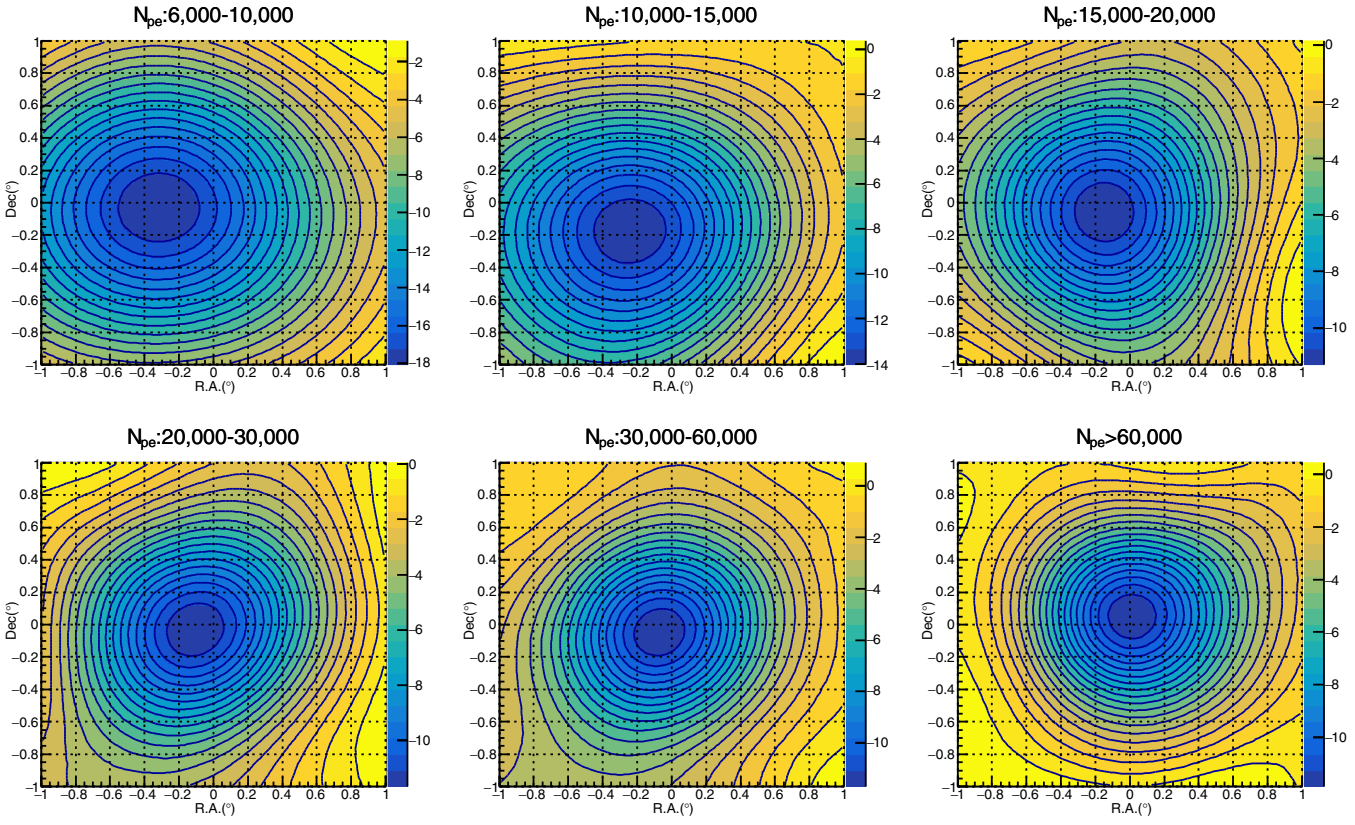

FIG. 5. The significance map of the Moon shadow for shower events detected by WCDA-1 of the six N_{pe} intervals. The coordinates are centered on the Moon position. The color scale represents the statistical significance of the deficit in terms of standard deviations.

direction through GMF. The interplanetary magnetic field, due to the solar wind, is by far less intense and can be neglected. The Tsyganenko-IGRF model [2] has been used to describe the magnetic field in the Earth-Moon system. We find that the displacement obtained applying this model can be described by the formula (1).

$$\Delta = 1.59°/R[\mathrm{TV}] \tag{1}$$

where R(TV) is the particle rigidity E(TeV)/Z. Thus the expected shift for Helium nuclei is a factor of 2 greater than the shift of protons of the same energy. However, for a given energy, the shower size N_e of Helium nuclei is less than the size of proton-induced shower. The median energies and trigger efficiencies of protons and Helium nuclei in a given N_{pe} interval, have been obtained by detailed simulations by CORSIKA v75000 [15] and detector responses. In CORSIKA v75000, the hadronic interaction models EPOS-LHC [16,17] and FLUKA [18] are selected above and below 100 GeV, respectively [7]. According to the simulation, in a given N_{pe} range, the median energy of Helium nuclei is 1.9 times that of protons, i.e., $E_{He} \approx 1.9E_P$. The rigidity of the Helium nuclei with the same shower size N_e of proton is then $R \approx 1.9E_P/2$, very close to the proton rigidity. This result has been already obtained in the Moon shadow analysis performed by ARGO-YBJ [1]. Thus, at a given selected interval of N_{pe}, corresponding to a shower size N_e interval, the displacement of Helium-induced showers is practically equal to that of showers generated by proton primaries. Moreover, fixing a N_{pe} interval we select a primary cosmic ray beam with the fraction protons: Helium nuclei is 2: 1 after triggering assuming the same flux for both components as measured by the CREAM [3] and DAMPE [4,5] experiments in this energy range. So the amount of the shift can be described by

$$\Delta = 2.1/E[\mathrm{TeV}] \tag{2}$$

where E is the median energy of the cosmic beam selected by fixing N_{pe}. This relation is shown in Fig. 6 where the deflection angles of proton and Helium nuclei pure beams are also reported for comparison. By using formula (2), the median energy of each N_{pe} selected interval reported in Table I can be obtained, which are shown in Fig. 6 by the squares with their statistic errors. Therefore, the energy scale can be fixed in the N_{pe} range 6,000 – 60,000 as shown in Fig. 7. The sixth N_{pe} interval is discarded in Fig. 7 due to its large statistic error. In the energy range from 6.6 TeV to 35.0 TeV N_{pe} can be used as energy proxy according to the relation $E[\mathrm{GeV}] = \mathrm{bN}_{\mathrm{pe}}^{\beta}$, $\beta = 0.95^{+0.18}_{-0.17}$ and $b = 1.33^{+5.29}_{-1.08}$.

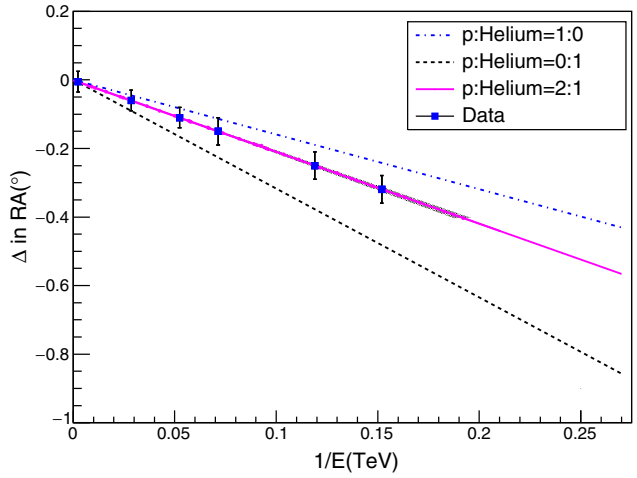

FIG. 6. The westward shift of the Moon shadow as a function of the inverse of the CR particle energy for pure protons (blue dot-dashed line) and pure Helium nuclei (black dashed line) according to the ray-tracing simulations. The pink solid line indicates the westward shift of the Moon shadow based on formula (2). The blue squares indicate the westward shifts of the Moon shadows with their statistical errors and the corresponding median energies obtained by formula (2). The uncertainty in the composition is represented by the shaded area around the pink solid line, however so small to be barely visible.

D. Uncertainties on energy scale

The uncertainty of the energy scale is mainly due to statistics, which determines the uncertainty on the measurement of Moon shadow shifts. The uncertainty on the position of the Moon shadow propagates to the energy scale being $d\Delta/\Delta = dE/E$. From Table I it can be seen that the average position of the shadow has an error of 0.04° in the lower energy bins, to become 0.03° at higher energies. These errors result in a rather large uncertainty in the energy scale reflected by the error bars reported in Fig. 7,

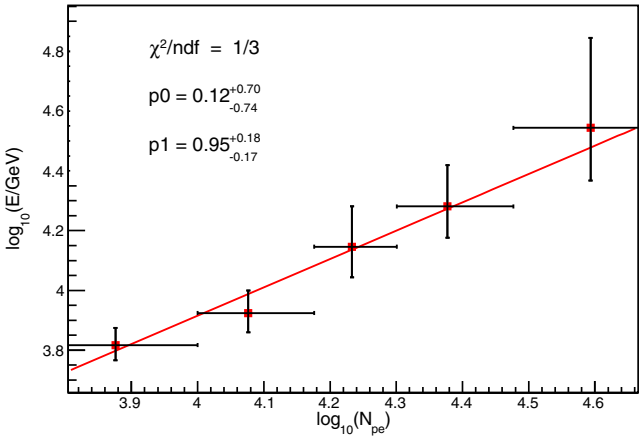

FIG. 7. The average shower energy measured using the Moon shadow shift versus N_{pe}, the total number of photoelectrons detected by WCDA-1 detector.

i.e., from 12% at 6.6 TeV to 50% at 35 TeV. These uncertainties are expected to drop to 3% and 12%, respectively, after four years of operations of the full WCDA detector.

Three systematic uncertainties may affect this analysis, one of them is the uncertainty on the ratio of protons to Helium nuclei, which is found about 3% with the ratio changing 10% over the energy range from 5 to 50 TeV according to the simulation. Another one is caused by the energy and angular resolution of the detector, about 4%. In addition, the uncertainties due to the choice of the hadronic interaction models such as EPOS-LHC [17] and QGSJET-II04 [19] are less than 2% according to the simulations.

IV. DETERMINATION OF THE ENERGY SCALE OF WFCTA

Using the GMF as a magnetic spectrometer, the absolute energy scale of WCDA-1 for the observation of protons and Helium nuclei has been calibrated. The calibration covers the energy range from 6 TeV to 35 TeV. This method, however, cannot be directly applied to calibrate the Cherenkov telescopes. To detect the faint Cherenkov light, WFCTA telescopes have to be operated on dark nights or at most with partial moonlight, thus avoiding having the Moon in the FoV and making it impossible to measure Moon shadow shifts for determining the energy scale.

Fortunately, WFCTA is installed next to WCDA, so hybrid observation is achieved. The energy scale of WCDA-1 obtained with the Moon shadow shifts can be used to provide a reference for the energy calibration of WFCTA. Using a set of commonly triggered events, the WCDA-1 energy scale can be compared with the energy reconstructed by WFCTA.

Due to the different energy thresholds, to the extension of the calibrated energy range and to the calibration uncertainties increasing with energy, this correlation is expected to be effective in a limited energy range around 20 TeV.

A. Commonly triggered data

Before 31/01/2020, there are about 2 months (Dec.2019 and Jan. 2020) for the WCDA-1 and WFCTA common operation. In the analysis, 10 nights in Jan. 2020 with moonless and very excellent weather conditions are selected.

The WFCTA telescopes are pointed at 30° in zenith direction, which results in a zenith angle coverage from 22° to 38°, taking into account the 16° FoV of the telescopes. Fig. 8 (lower) shows the distribution of zenith angles of commonly triggered events with the center of gravity of the Cherenkov images within 5° from the camera center. Figure 8 (upper) shows the distributions of N_{pe} for events with zenith angle $22° < \theta_z < 38°$ (by the blue solid line) and for the commonly triggered events (by the red dashed line) with at least 2 triggered pixels and 50 pe single threshold of WFCTA.

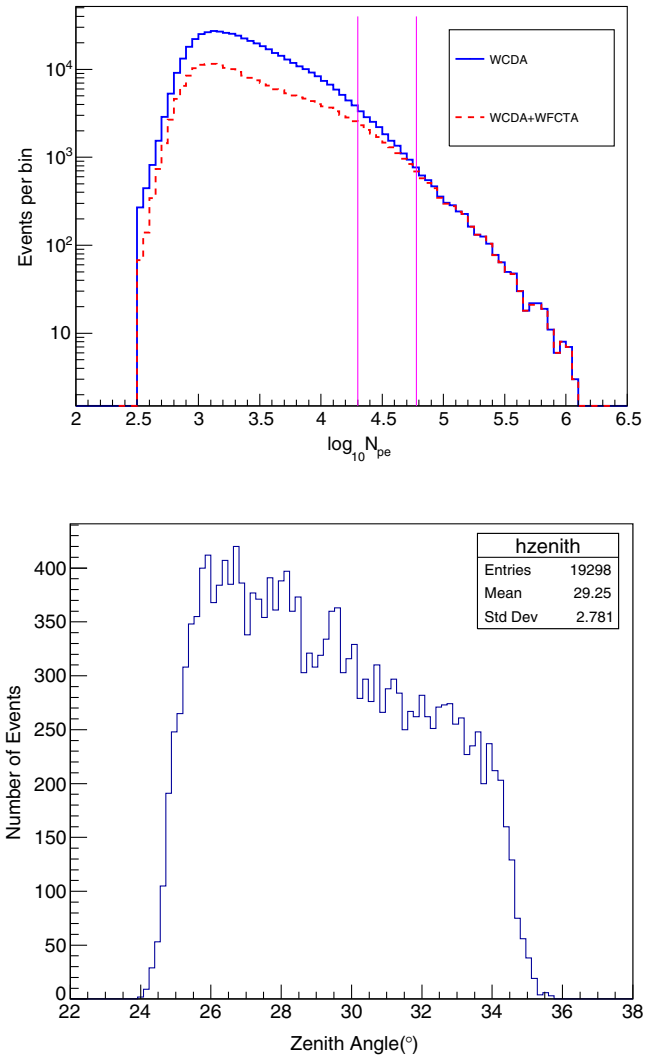

FIG. 8. Upper: distribution of N_{pe} for the events with cores inside WCDA-1 with zenith angle $22° < \theta_z < 38°$ (by the blue solid line) compared to the N_{pe} distribution for the commonly triggered events (by the red solid line). In the selected region of N_{pe}, denoted by the vertical lines, the selection efficiency is high enough to have almost the same ratio protons: Helium nuclei $= 2:1$. Lower: distribution of the zenith angles for the commonly triggered events.

Looking at the distributions in Fig. 8, it can be seen that WCFTA triggers 100% of WCDA-1 events only for N_{pe} above 60,000, and that the efficiency drops below 75% for N_{pe} below 20,000. This is due to the fact that the trigger efficiency of WCFTA telescopes decreases with increasing distance from the shower core and also for decreasing energy. On the contrary, the Moon shadow shift is better reconstructed for lower energies ($N_{pe} < 60{,}000$).

Therefore, the common dataset has been selected choosing the best compromise using the following criteria: $N_{hit} > 200$, $20{,}000 < N_{pe} < 60{,}000$ and $22° < \theta_z < 38°$.

B. Energy reconstruction of WFCTA

The density of Cherenkov photons produced during the shower development is proportional to the primary particle energy. Therefore a good estimator of the energy for WFCTA data is the sum of the number of photoelectrons in the camera image, $\sum$, once corrected for geometric effects. The quantity $\sum$ is usually called the *size of the image*, in the traditional shower energy reconstruction scheme [20,21] for Cherenkov telescopes. The correction on $\sum$ includes its dependence on the viewing angle a, the space angle between the shower direction and the main axis of the telescope, and the perpendicular distance, R_p, from the shower axis to the telescope in shower-detector-plane. The R_p correction takes into account the fact that photon density decreases with increasing distance from the shower core. The viewing angle a correction is due to the weakening of the shower image on the camera for off-axis showers. This is a combination of the shadow of the container in which the telescope is installed and the reduced effective area of the mirror for off-axis showers. The correction has been calculated with a detailed simulation of the WFCTA telescopes response [22] normalizing the measured $\sum$ to $R_p = 0$ and $a = 0$. The shower energy can be estimated from the corrected $\sum$.

The relationship between $\sum$ and the primary energy of cosmic rays can be obtained by simulations of air showers and WFCTA telescope response. In the simulation, the primary flux of protons and Helium nuclei is assumed to be 1:1. Under the assumption, the energy resolution is 20% for showers with energies below 100 TeV, and 15% above 100 TeV with a systematic shift less than 5% [22].

The shower core should be located well inside WCDA-1 to obtain good the energy resolution. So in addition to the previous selection criteria used to determine a common dataset, a constraint concerning a shower core location well inside WCDA-1 has been added by requiring $|x_{\rm core}| < 55$ m and $|y_{\rm core}| < 55$ m, where $x_{\rm core}$ and $y_{\rm core}$ are the distance of the shower core from the center of WCDA-1. In addition, for good detection and to reduce the correction of Σ for variation in R_p and a, the WFCTA events are required to be not too far, i.e., $R_p < 100$ m, to have at least 2 triggered pixels with 82 pe offline threshold cut, and to have the center of gravity of the images within 5° from the camera center. The distribution of energies, $E_{\rm WFCTA}$ reconstructed by $\sum$ for the sample selected with these cuts is shown in Fig. 9. The median value (21.9 ± 0.1 TeV) of the distribution is shown by the vertical red solid line.

C. Energy scale propagation from WCDA-1 to WFCTA

The WCDA-derived energies for commonly triggered events with the same cuts can be reconstructed by the formula $E[\mathrm{GeV}] = 1.33\, N_{\rm pe}^{0.95}$, and are shown in Fig. 9 by the black dashed line. The median value ($23.4 \pm 0.1 \pm 1.3$ TeV) of the distribution is shown by the vertical black dashed line. Here, 0.1 TeV is the statistical uncertainty, while 1.3 TeV is the systematic uncertainty caused by the errors on the b and β parameters in the absolute energy scale formula. Comparing the two median energies derived from WFCTA and WCDA-1, they are consistent with each other considering the uncertainties. So far, we have managed to calibrate the energy scale of WFCTA by the commonly dataset.

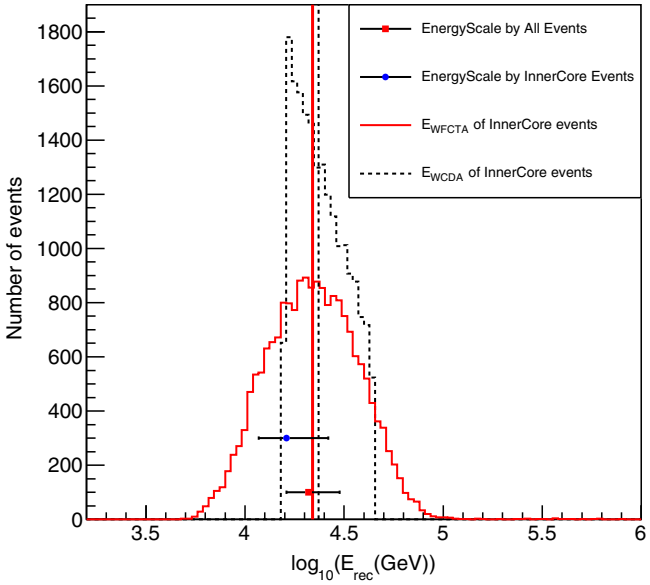

FIG. 9. Distribution of reconstructed energies for the commonly triggered events. The black dashed line shows the energy distribution reconstructed by WCDA-1 using the estimator $E[\mathrm{GeV}] = 1.33 \cdot \mathrm{N}_{\rm pe}^{0.95}$. The vertical black dashed line indicates the median energy ($23.4 \pm 0.1 \pm 1.3$ TeV) of the distribution. The continuous red solid line shows the distribution of the energies reconstructed by the WFCTA telescopes. The vertical red solid line indicates the median energy (21.9 ± 0.1 TeV) of the distribution. The median energies $21.0^{+9.0}_{-4.8}$ TeV and $16.2^{+10.1}_{-4.5}$ TeV obtained from the Moon shadow data are shown by a red square and a blue dot, respectively. The first energy is related to the selection $N_{\rm hit} > 200$, $20{,}000 < N_{\rm pe} < 60{,}000$, $22° < \theta_z < 38°$, the second one by requiring in addition the shower core falling inside WCDA-1.

D. Validation of energy scale using Moon shadow shift

The events used to determine the WCDA-1 energy scale in Sec. IV, come from a region defined by the zenith angle θ_z interval, 10° to 45°. The event distribution as a function of the zenith angles accepted in the WCDA-1 Moon shadow analysis is reported in Fig. 10(upper). The shaded areas represent the zenith angle portion not accessible to WFCTA. To test the energy scale of the commonly triggered events, the commonly triggered events are reanalyzed to calculate the Moon shadows.

A new significance map of the Moon shadow with these selection criteria is obtained, shown in Fig. 10

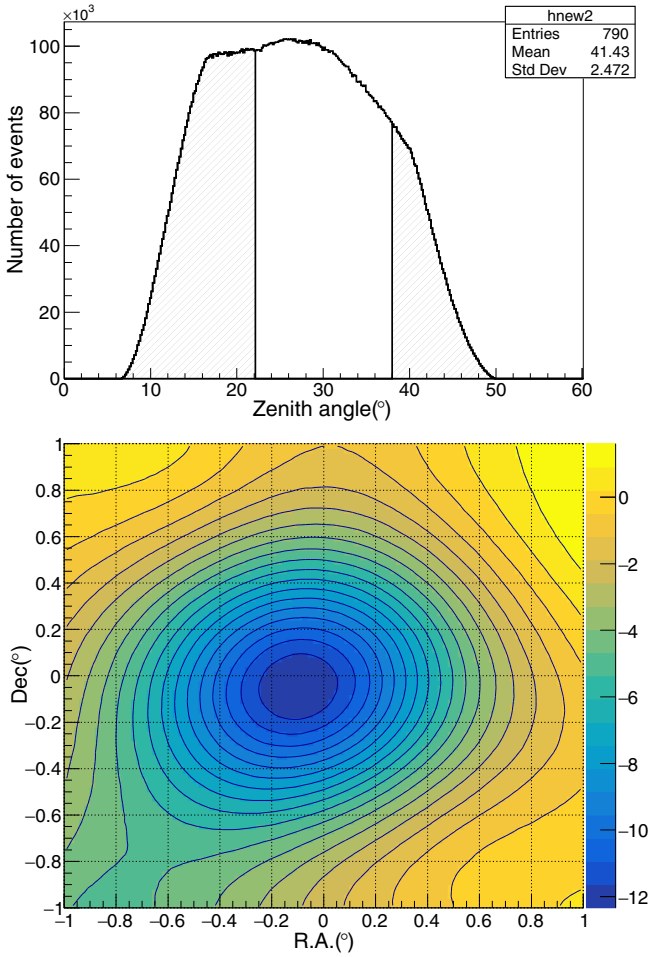

FIG. 10. Upper: the distribution of zenith angles of all events with $N_{\rm hit} > 200$ used in the WCDA-1 Moon shadow analysis. The shaded areas represent the zenith range not covered by WFCTA telescopes. Lower: the significance map of the Moon shadows, for events with $N_{\rm pe}$ between 20,000 and 60,000 and in the zenith angle range covered by the WFCTA telescopes, i.e., $22° \le \theta_z \le 38°$. The color scale represents the statistical significance of the deficit in terms of standard deviations.

(lower). The value obtained for the shift in this case is $\Delta = (0.10 \pm 0.03)°$, which translates to an energy $21.0^{+9.0}_{-4.8}$ TeV, using the formula $\Delta = 2.1/E[\mathrm{TeV}]$ as before. The quoted uncertainty of about 30% is purely statistical. Considering the uncertainty, the energy is consistent with the energy scale of the commonly data.

In order to evaluate the bias introduced by the requirement to have the shower core well inside WCDA, the energy has been estimated by the Moon dataset adding the conditions $|x_{\rm core}| < 55$ m and $|y_{\rm core}| < 55$ m to the previous ones, i.e., $N_{\rm hit} > 200$, $20{,}000 < N_{\rm pe} < 60{,}000$ and $22° < \theta_z < 38°$. The resulting deflection angle is $\Delta = (0.13 \pm 0.05)°$, which translates into an energy of $16.2^{+10.1}_{-4.5}$ TeV, according to the formula $\Delta = 2.1/E(\mathrm{TeV})$, with a relative uncertainty of about 38%. This is shown in Fig. 9 by a blue dot with its error. The change of the energy

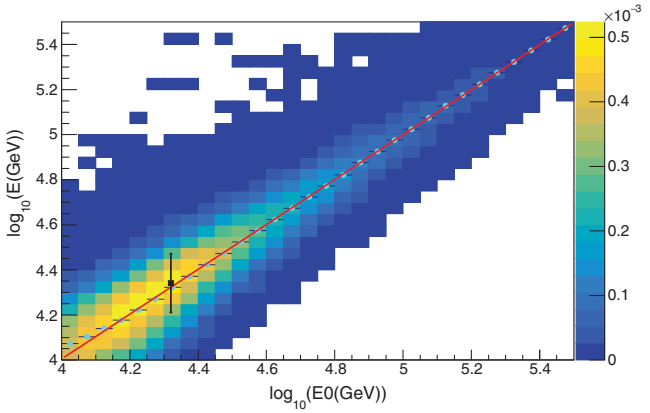

FIG. 11. The relation in the energy range 10–300 TeV between the energy estimator $E_{\rm WFCTA}$ of WFCTA and the energy E_0 of primary protons and Helium nuclei sample according to the ratio protons: Helium nuclei = 1: 1, based on the simulations of WFCTA telescopes. The red line represents the median energy of the $E_{\rm WFCTA}$ distribution. The black square indicates the corresponding value of the energy, $21.0^{+9.0}_{-4.8}$ TeV, determined by WCDA-1 from the Moon shadow shift. The color scale gives the number of events in each bin. The width bin is $d\log_{10}E_0 = 0.05$.

scale introduced by the further requirement of having the shower core well within WCDA-1 is about 30%.

In few years LHAASO will accumulate huge statistics allowing a substantial reduction of the uncertainty on the energy scale.

To extrapolate the WFCTA energy scale as determined in the overlapping region with WCDA-1, the correspondence between the energy estimator of WFCTA and the primary energy has been checked using simulations of WFCTA telescopes. Figure 11 shows the distribution of $E_{\rm WFCTA}$ reconstructed by WFCTA as a function of the input primary energy E_0, spanning a range from 30 TeV to 300 TeV. In addition, the energy scale determined from the Moon shadow shift measured by WCDA-1 is reported by a black square together with the error bar at $21.0^{+9.0}_{-4.8}$ TeV. For showers with greater energy the energy reconstruction totally relies on the simulation of air showers and detector response of WFCTA.

V. CONCLUSIONS

In this work, we have shown how the shift of the Moon shadow cast by cosmic rays, due to the geomagnetic field, can be used to establish the energy scale of the WCDA-1 detector in the range from 6 TeV to 35 TeV, using the estimator $E[\mathrm{GeV}] = 1.33 \cdot \mathrm{N}_{\rm pe}^{0.95}$, based on the total number of photoelectrons $N_{\rm pe}$ measured in the pond. The uncertainty of the energy scale varies from 12% at 6.6 TeV to 50% at 35 TeV and is dominated by statistical errors. The systematic error coming from the assumption concerning the ratio protons and Helium nuclei as determined by space

born experiments [3] has been shown to be about 3%. The combination of the energy and angular resolution of WCDA-1 introduces extra 4% uncertainty in matching the median energy with the median deflecting angle. The systematic uncertainty related to the use of different hadronic interaction models is found less than 2%.

Given the impossibility to measure the Moon shadow shift directly with WFCTA, a set of events commonly triggered with WCDA-1 has been used to correlate the energy scale of WCDA-1 to the measurement using WFCTA telescopes. The two types of detector have different energy thresholds, and this overlap occurs in a limited energy range of WCDA-1, where the Moon shadow shift method results in a rather large uncertainty of about 30% on the "common" energy scale. As a matter of fact, this uncertainty is largely dominated by the low statistics of events. The propagation of the energy scale measured by WCDA-1 to WFCTA is established through a set of commonly triggered events by both WFCTA telescopes and WCDA-1 with the selection criteria $N_{\rm hit} > 200$, $20{,}000 < N_{\rm pe} < 60{,}000$, $22° < \theta_z < 38°$ and $|x_{\rm core}| < 55$ m and $|y_{\rm core}| < 55$ m. With these selection criteria, the median energy reconstructed by WFCTA is found to be 21.9 ± 0.1 TeV, while the median energy derived from $E[\mathrm{GeV}] = 1.33 \cdot \mathrm{N}_{\rm pe}^{0.95}$ is $23.4 \pm 0.1 \pm 1.3$ TeV, the two median energies are consist with each other within uncertainties. In addition, the propagation of the energy scale is also validated by the Moon shadow based on the same data selection criteria of the commonly triggered events. This is the first report of an observational measurement of the absolute energy scale of the primary cosmic rays generating showers observed by air Cherenkov telescopes.

ACKNOWLEDGMENTS

The authors would like to thank all staff members who work at the LHAASO site all year around to keep the system running efficiently and smoothly, even in the demanding conditions at a mean altitude of 4400 meters above sea level. We are grateful to the Chengdu Management Committee of Tianfu New Area for the constant financial support to the research with LHAASO data. This research work is also supported by the National Key R&D program of China, with the Grants No. 2018YFA0404201, No. 2018YFA0404202, and No. 2018YFA0404203, the National Natural Science Foundation of China, with NSFC Grants No. 11635011, No. 11761141001, No. 11905240, No. 11503021, No. 11205126, No. 11947404, No. 11675187, No. U1831208, Schools of Science and Technology Plan from SiChuan Province Grant No. 20SYSX0294, and Thailand Science Research and Innovation Grant No. RTA6280002.

[1] B. Bartoli *et al.* (ARGO-YBJ Collaboration), Phys. Rev. D **84**, 022003 (2011).
[2] N. A. Tsyganenko, J. Geophys. Res. **100**, 5599 (1995).
[3] Y. S. Yoon *et al.*, Astrophys. J. **839**, 5 (2017).
[4] Q. An *et al.* (DAMPE Collaboration), Sci. Adv. **5**, eaax3793 (2019).
[5] F. Alemanno *et al.*, Phys. Rev. Lett. **126**, 201102 (2021).
[6] H. He (for LHAASO Collaboration), Radiat. Detection Technol. Methods **2**, 7 (2018).
[7] F. Aharonian *et al.*, arXiv:2101.03508v1.
[8] C. A. O. Zhen (for LHAASO Collaboration), Chin. Phys. C **34**, 249 (2010).
[9] F. Aharonian *et al.*, Chin. Phys. C **45**, 025002 (2021).
[10] B. Bi, S. Zhang, Z. Cao, L. Yin, L. Ma, C. Wang, T. Montaruli, D. della Volpe, and M. Heller (for LHAASO Collaboration), Nucl. Instrum. Methods Phys. Res., Sect. A **899**, 94 (2018).
[11] C. R. Benn, arXiv:astro-ph/9909153v1.
[12] F. Aharonian *et al.*, Eur. Phys. J. C **81**, 657 (2021).
[13] M. Amenomori *et al.*, Astrophys. J. **633**, 1005 (2005).
[14] T. P. Li and Y. Q. Ma, Astrophys. J. **272**, 317 (1983).
[15] D. Heck *et al.*, Report No. FZKA 6019, 1998.
[16] T. Pierog and K. Werner, Nucl. Phys. B, Proc. Suppl. **196**, 102 (2009).
[17] T. Pierog, I. Karpenko, J. M. Katzy, E. Yatsenko, and K. Werner, Phys. Rev. C **92**, 034906 (2015).
[18] A. Fassò, A. Ferrari, and S. Roesler, arXiv:hep-ph/0306267.
[19] S. S. Ostapchenko, Phys. Rev. D **83**, 014018 (2011).
[20] A. M. Hillas, Annu. Rev. Astron. Astrophys. **22**, 425 (1984).
[21] B. Bartoli *et al.*, Phys. Rev. D **92**, 092005 (2015).
[22] L. Q. Yin *et al.*, Chin. Phys. C **43**, 075001 (2019).